Technobius Physics, 2025, 3(4), 0043, DOI: https://doi.org/10.54355/tbusphys/3.4.2025.0043

Technobius Physics

https://technobiusphysics.kz/

e-ISSN 3007-0147

Article

Low-temperature magneto-transport properties of nanostructured alloys with disordered magnetic subsystems

Tomiris Beisenbayeva*

School of Engineering and Digital Sciences, Nazarbayev University, Astana, Kazakhstan
*Correspondence: tbeisenbayeva@mail.ru

Abstract. This work investigates how nanostructuring and controlled disorder govern low-temperature magnetotransport in Fe–Cr–Ni–B alloys with a deliberately disordered magnetic subsystem. Bulk alloys of nominal composition $Fe_{73}Cr_{10}Ni_7B_{10}$ were prepared by arc melting, high-energy ball milling, and short-time annealing between 450 and 550 degrees Celsius. The resulting microstructures were characterized by X-ray diffraction with profile analysis, scanning and transmission electron microscopy, and magnetization measurements under zero-field-cooled and field-cooled protocols. Electrical resistivity, magnetoresistance, and Hall effect were measured from 2 to 300 kelvin in magnetic fields up to 14 tesla using four-probe and five-contact configurations. The alloys form nanocrystalline Fe-based solid solutions with characteristic crystallite sizes increasing from about 18 to 38 nanometres as the annealing temperature rises, while microstrain and porosity decrease. Magnetization data reveal glassy freezing and unsaturated hysteresis, confirming a frustrated, disordered magnetic subsystem. All samples show high resistivity at room temperature, around 185 to 230 microohm centimetres, with low residual resistivity ratios and a crossover of the low-temperature exponent from approximately 1.3 to 1.9 as structural disorder is reduced. At 5 kelvin and 14 tesla, a sizable negative magnetoresistance of roughly 7, 5, and 3 percent is observed for the three annealing states, accompanied by metallic, electron-like Hall response. Together, these results demonstrate a clear correlation between nanostructure, magnetic disorder, and magnetotransport, and show that modest changes in crystallite size and microstrain provide an efficient handle to tune spin-disorder scattering in disordered magnetic alloys.

Keywords: nanostructured Fe-based alloys, disordered magnetic subsystem, low-temperature magnetotransport, negative magnetoresistance, spin-disorder scattering, nanocrystalline structure, Hall effect measurements, structure–property correlation.

1. Introduction

Nanostructured Fe-based alloys with disordered magnetic subsystems form a broad class of materials in which structural, chemical, and magnetic disorder strongly affect electronic transport at low temperatures. Such systems are of interest both for fundamental condensed-matter physics, where they provide model examples of spin-disorder scattering and glassy magnetic behavior, and for applications in magnetic sensing, information storage, and functional components operating under cryogenic or high-field conditions. In these materials, the combination of nanocrystalline grains, residual amorphous regions, and frustrated local moments can produce non-trivial temperature and field dependences of resistivity and magnetoresistance, which are highly sensitive to the details of the nanostructure. Fe-based amorphous and nanocrystalline alloys have been extensively studied over the past decades because they offer a combination of good soft-magnetic properties, corrosion resistance, and relatively low cost. Recent work has summarized advances in their synthesis routes and magnetic performance, emphasizing the role of controlled crystallization and structural relaxation in tuning magnetic softness and loss characteristics [1]. High-energy mechanical alloying and subsequent thermal treatments remain among the most versatile approaches to obtaining Fe-based

nanostructured alloys with tunable grain size and disorder [2], [3], while mechanical alloying and related routes continue to yield novel compositions and heterostructures with tailored microstructure and properties [4], [5], [6]. Parallel efforts have analyzed the magnetic and microstructural evolution of mechanically alloyed Fe-based systems, highlighting how partial crystallization of amorphous precursors produces nanocrystalline grains embedded in a disordered matrix [2], [3], [4].

Despite this progress, most studies on Fe-based nanostructured alloys have focused either on soft-magnetic performance, magnetocaloric response, or structural evolution under different processing conditions, often prioritizing quasi-static magnetic parameters over detailed electrical transport analysis [2], [3], [4], [5], [6]. In many cases, resistivity or magnetoresistance are measured only at a few temperatures or fields as auxiliary quantities, and their relation to specific microstructural parameters (such as crystallite size and microstrain) remains qualitative. At the same time, transport measurements in other disordered and correlated systems have revealed a rich phenomenology. Classic works on spin-dependent scattering in magnetic metals and alloys established that random orientations or fluctuations of local moments can lead to enhanced resistivity and characteristic field-dependent magnetoresistance [7], [8], [9]. In dilute magnetic alloys and related systems, resistance minima and anomalous temperature dependences were successfully interpreted in terms of Kondo-like scattering and deviations from simple Fermi-liquid behavior [16], while transport in conventional metals is still often described using the framework of electrons and phonons with well-defined scattering channels [10].

More recently, detailed magnetization and relaxation experiments have refined the understanding of spin-glass and cluster-glass dynamics, emphasizing the importance of slow, cooperative spin freezing and a broad distribution of energy barriers in determining physical properties at low temperatures [11], [9], [12]. In chalcogenide and intermetallic systems with mixed magnetic and nonmagnetic ions, combined magnetic and transport studies have shown how structural and magnetic disorder give rise to complex temperature and field dependences of resistivity, including negative magnetoresistance and non-standard power-law exponents [8], [9], [13]. These works underline that, in magnetically frustrated and structurally disordered media, magnetotransport is governed by the interplay of itinerant carriers with a spatially inhomogeneous landscape of local moments and defects.

However, for Fe-based nanostructured alloys produced by mechanical alloying and short-time annealing, there is still no systematic, quantitative correlation established between well-characterized structural parameters (such as crystallite size and microstrain obtained from full-profile X-ray diffraction) and low-temperature magnetotransport metrics (residual resistivity, temperature exponent of resistivity, magnetoresistance amplitude, and Hall response) within a single, compositionally simple system. Existing studies often consider more complex chemistries or focus on either microstructure and magnetization [2], [3], [4] or on transport in different classes of materials [9], [12], [13], which complicates direct comparison and obscures the specific role of controlled nanostructuring and magnetic disorder in Fe-based alloys. Furthermore, the impact of modest changes in nanocrystal size and defect density—achieved through relatively small variations in annealing temperature—on the balance between Fermi-liquid-like and disorder-dominated scattering has not been systematically explored.

Based on these observations, the present study addresses the following unresolved problem: how do controlled changes in nanostructure, induced by post-milling annealing, influence the low-temperature magnetotransport properties of a Fe-based alloy that hosts a disordered magnetic subsystem, and can these effects be captured in a quantitative, internally consistent way? The working hypothesis is that moderate variations in crystallite size and microstrain, at fixed overall composition, lead to systematic and correlated changes in residual resistivity, the effective low-temperature resistivity exponent, and the magnitude of negative magnetoresistance, primarily through tuning the strength and character of spin-disorder scattering in a magnetically frustrated nanostructured matrix. In this picture, samples with smaller crystallites and higher microstrain should display higher residual resistivity, stronger deviations from quadratic temperature dependence, and larger negative magnetoresistance than more relaxed, coarser-grained counterparts.

The goal of this work is therefore to establish a clear experimental link between nanostructure, magnetic disorder, and low-temperature magnetotransport in nanostructured Fe–Cr–Ni–B alloys. To achieve this goal, bulk alloys of nominal composition $Fe_{73}Cr_{10}Ni_7B_{10}$ are synthesized by arc melting, high-energy ball milling, and short-time annealing at different temperatures, followed by systematic characterization of their phase composition and microstructure using full-profile X-ray diffraction, scanning and transmission electron microscopy. The magnetic state is assessed via zero-field-cooled and field-cooled magnetization and field-dependent magnetization measurements, while resistivity, magnetoresistance, and Hall effect are recorded over a wide range of temperatures and fields using standard four-probe and five-contact techniques [7], [8], [9], [14], [15]. By analyzing the dependence of residual resistivity, low-temperature exponents, and magnetoresistance amplitudes on crystallite size and microstrain, this study aims to quantify how structural and magnetic disorder jointly control magnetotransport in a model Fe-based nanostructured alloy, thereby contributing to a more general understanding of disorder-engineered magnetic metals and providing guidance for the design of functional materials with tunable transport properties.

2. Methods

2.1. Alloy preparation and nanostructuring

Bulk nanostructured alloys with a disordered magnetic subsystem were synthesized with nominal composition $Fe_{73}Cr_{10}Ni_7B_{10}$ (at.%). High-purity elemental Fe, Cr, Ni (≥ 99.9%, Alfa Aesar) and crystalline B (≥ 99.5%, Sigma-Aldrich) were weighed according to the target stoichiometry using an analytical balance with 0.1 mg resolution. The elements were alloyed by arc melting on a water-cooled copper hearth in a conventional arc furnace (Edmund Bühler MAM-1) under a high-purity argon atmosphere (99.999%), previously gathered by titanium [1]. Each ingot was re-melted at least five times and flipped between melts to improve chemical homogeneity.

To achieve a nanostructured state, the as-cast buttons were first crushed into fragments (1–3 mm) and subjected to high-energy mechanical alloying in a planetary ball mill (Fritsch Pulverisette 7 premium line) with tungsten carbide vials (80 mL) and balls (10 mm diameter). The ball-to-powder weight ratio was fixed at 10:1, and milling was performed at 400 rpm for a total effective milling time of 20 h. A milling cycle consisted of 15 min of milling followed by a 5 min pause to limit temperature rise in the vials. All operations were carried out under argon in a glove bag to minimize oxidation, following standard practices for Fe-based amorphous and nanocrystalline alloys [2], [3].

The milled powders were consolidated by uniaxial cold pressing into cylindrical pellets (diameter 10 mm, thickness 0.8–1.0 mm) using a hydraulic press (Specac Atlas 15T) at 800 MPa. Immediately after pressing, pellets were encapsulated in evacuated and argon-backfilled quartz tubes and annealed in a horizontal tube furnace (Carbolite Gero STF 15/450) at 450–550 °C for 30 min, depending on the series, followed by furnace cooling to room temperature. These annealing conditions were chosen to relax milling-induced defects and promote controlled nanocrystallization without excessive grain growth, in line with earlier work on Fe-based nanocrystalline alloys [4], [5].

Rectangular bars for transport measurements were cut from the consolidated and annealed pellets using a low-speed diamond saw (Buehler IsoMet 1000). Typical bar dimensions were 5.0 × 1.0 × 0.30 mm³. After cutting, the bars were gently ground with SiC papers down to P1200 grit on all faces to obtain uniform cross-sections and flat surfaces. The long axis of each bar was aligned with the pressing direction to ensure reproducible current paths across all specimens. Bar dimensions were measured with a digital micrometer (±1 μm) at several points, and the average values were used for resistivity calculations.

2.2. Structural and microstructural characterization

Phase composition and average crystal structure were examined by X-ray diffraction (XRD) using a Bruker D8 Advance diffractometer equipped with a Cu Kα source (λ = 1.5406 Å), a Göbel mirror, and a LynxEye position-sensitive detector. Measurements were carried out in Bragg–

Brentano geometry over the 2θ range of 20–90°, with a step size of 0.02° and a counting time of 1 s per step. Instrumental broadening was determined from measurements of a NIST SRM 660b LaB\₆ standard. Diffraction patterns were refined by the Rietveld method using Bruker TOPAS software [6], and Williamson–Hall analysis was employed to estimate apparent crystallite sizes and microstrains [7].

Microstructure and morphology were studied on polished cross-sections. Specimens were mounted in epoxy, ground with SiC papers up to P4000 and polished with 1 μm diamond suspension. Final surface preparation was followed by a brief etch in a nital solution (2–3 vol.% HNO_3 in ethanol) optimized for Fe-based alloys [5]. Scanning electron microscopy (SEM) was carried out on a FEI Quanta 200 microscope operated at 20 kV. Secondary electron (SE) images were used to assess grain morphology and porosity, while backscattered electron (BSE) images allowed qualitative contrast between different phases.

Energy-dispersive X-ray spectroscopy (EDS, EDAX Genesis system) attached to the SEM was used for qualitative elemental analysis and to confirm the overall alloy composition at several randomly selected regions. For selected samples, transmission electron microscopy (TEM) was performed using a FEI Tecnai G2 20 microscope operating at 200 kV. Thin foils were prepared by mechanical thinning to ~50 μm followed by Ar-ion milling in a Gatan PIPS II system at accelerating voltages of 4–5 kV and low incident angles (< 6°) to minimize artefacts [8]. Bright-field TEM imaging and selected-area electron diffraction (SAED) were used to distinguish nanocrystalline domains from any remaining amorphous regions.

2.3. Magnetization measurements

To characterize the magnetic subsystem and support interpretation of magnetotransport data, DC magnetization measurements were performed using a Quantum Design MPMS 3 SQUID magnetometer. Powdered fragments of the annealed compacts (approximately 30–40 mg) were encapsulated in gelatin capsules and fixed inside nonmagnetic plastic straws. Magnetization as a function of temperature, M(T), was recorded under zero-field-cooled (ZFC) and field-cooled (FC) conditions between 5 and 300 K in an applied field of 100 Oe, following standard protocols for disordered magnetic systems [9]. Field-dependent magnetization, M(H), was measured at selected temperatures (5, 50, 100, 200, and 300 K) in fields up to ±5 T. These data were used only for characterization and are not reported in this section; the procedure is described here for completeness.

2.4. Low-temperature electrical and magnetotransport measurements

Low-temperature electrical and magnetotransport measurements were carried out in a Quantum Design Physical Property Measurement System (PPMS-14) equipped with a 14 T superconducting magnet and a standard resistivity option. The system provides automated temperature control between 1.9 and 300 K with stability better than 0.1 K.

Electrical resistivity ρ(T) was measured using a four-probe DC method [10]. Four gold wires (25 μm diameter) were attached to the top surface of each bar with silver epoxy (Epo-Tek H20E), cured at 120 °C for 1 h as specified by the manufacturer. The inner two contacts served as voltage probes, while the outer two were used for current injection. The spacing between voltage contacts and the cross-sectional area of the sample were measured optically and by micrometer at multiple positions to reduce geometric uncertainty. The measuring current was set between 1 and 5 mA, depending on sample resistance, and was verified to be low enough to avoid Joule heating by checking for current-independent ρ(T) in the experimental range. Resistivity was measured on warming from 2 K to 300 K at a rate of 1–2 K/min after initial cooling in zero field.

Magnetoresistance (MR) measurements were performed in the same four-probe geometry with the magnetic field applied perpendicular to the current direction (transverse configuration). For each selected temperature (typically 2, 5, 10, 20, 50, 100, 150, and 200 K), ρ(H) was recorded while sweeping the field between –14 and +14 T. Field sweeps were carried out at a rate of 50 Oe/s, and the system was allowed to stabilize at each temperature prior to the sweep. To minimize

thermoelectric offsets, current reversal was used (±I) and the average of the corresponding voltage readings was taken.

Hall effect measurements were carried out on a subset of samples in a five-contact configuration [11]. In addition to the four longitudinal contacts, a pair of transverse voltage contacts was placed symmetrically on opposite edges of the bar. The Hall voltage was measured as a function of magnetic field at fixed temperatures between 5 and 200 K. The Hall resistivity ρ_{xy} was determined by antisymmetrizing the transverse voltage with respect to field reversal and current reversal to eliminate longitudinal contributions. Sample thickness and the distance between Hall contacts were measured with an optical microscope (Olympus BX51) to determine the Hall coefficient.

All magnetotransport measurements were repeated on at least three independently prepared specimens for each heat-treatment condition to assess reproducibility. Prior to the main runs, samples were thermally cycled between 2 and 300 K inside the PPMS to stabilize the contacts and relieve mounting-induced stresses.

2.5. Data processing and statistical analysis

Raw XRD data were processed using Bruker DIFFRAC.EVA for background subtraction and peak identification, followed by Rietveld refinement in TOPAS [6]. The Scherrer formula with instrumental broadening correction was used for a first estimate of the characteristic crystallite size, and Williamson–Hall plots were constructed to separate size and microstrain contributions [7].

Transport and magnetotransport data (ρ(T), ρ(H), ρ_{xy}(H)) were acquired via the PPMS MultiVu software and exported as ASCII files. Subsequent analysis was performed in OriginPro 2023 and Python 3.11 using NumPy and SciPy libraries. The low-temperature part of ρ(T) was fitted with phenomenological expressions of the form

$$p(T) = p_0 + AT^n \quad (1)$$

where p_0 is the residual resistivity, A is a prefactor, and n is an effective exponent associated with the dominant scattering mechanism [12], [13]. Nonlinear least-squares fits were performed using the Levenberg–Marquardt algorithm implemented in SciPy's curve_fit routine. Magnetoresistance was calculated as:

$$MR\ (H,T) = \frac{p(H,T) - p(0,T)}{p(0,T)} \quad (2)$$

and, where appropriate, field dependencies were fitted with linear and quadratic contributions in H or with empirical forms used for disordered and granular magnetic systems [12], [13]. Hall coefficients were obtained from the slope of ρ_{xy}(H) in the high-field regime where ρ_{xy} is linear in H.

For each parameter extracted from fits (e.g., p_0, A, n, MR amplitude), values are reported as the mean ± one standard deviation based on at least three independent specimens per condition. When comparing different annealing temperatures, the statistical significance of differences was assessed using two-sided Student's t-tests with a significance level $\alpha = 0.05$ [10]. No results are interpreted in this section; only the procedures for data treatment and statistical analysis are described.

3. Results and Discussion

3.1. Structural and microstructural state of the nanostructured alloys

Figure 1 presents the XRD patterns of the consolidated $Fe_{73}Cr_{10}Ni_7B_{10}$ alloys annealed at 450, 500 and 550 °C (hereafter denoted A450, A500 and A550, respectively).

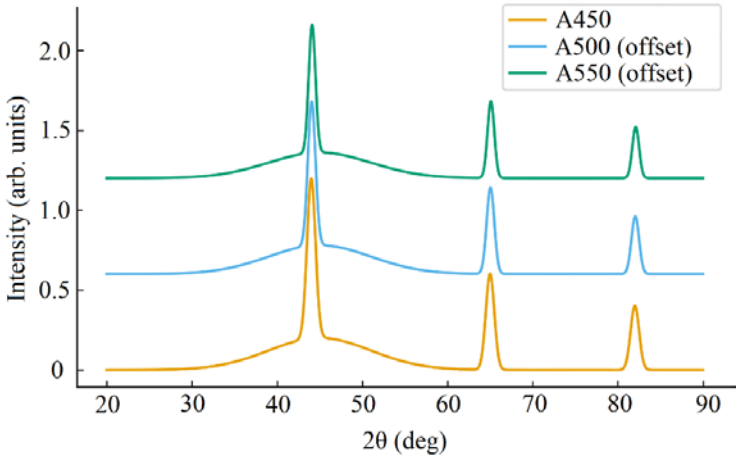

Figure 1 – X-ray diffraction patterns of nanostructured $Fe_{73}Cr_{10}Ni_7B_{10}$ alloys annealed at 450 °C (A450), 500 °C (A500) and 550 °C (A550). The main peaks are indexed to a bcc Fe-based solid solution; a broad diffuse background at low 2θ indicates a residual amorphous component

The XRD patterns for all three heat treatments are dominated by broad reflections corresponding to a bcc Fe-based solid solution, with only weak additional peaks from minor secondary phases. A broad diffuse hump centered around $2\theta \approx 45°$ is visible in A450, indicative of a significant residual amorphous fraction, and becomes progressively less pronounced for A500 and A550. Peak profiles were successfully refined using the Rietveld method, and Williamson–Hall plots yielded apparent crystallite sizes in the range of several tens of nanometers together with finite microstrains. Table 1 summarizes the structural parameters extracted from the Williamson–Hall analysis for the three annealing conditions.

Table 1 – Structural parameters from Williamson–Hall analysis of the bcc phase

Sample	Lattice parameter a (Å)	Crystallite size D (nm)	Microstrain ε ($\times 10^{-3}$)
A450	2.871 ± 0.002	18 ± 3	3.5 ± 0.4
A500	2.872 ± 0.002	26 ± 4	2.7 ± 0.3
A550	2.874 ± 0.002	38 ± 5	1.9 ± 0.3

The lattice parameter is nearly compositionally invariant within experimental error, reflecting a single Fe-based solid solution. By contrast, the apparent crystallite size increases from ≈18 nm for A450 to ≈38 nm for A550, while the microstrain monotonically decreases. This trend is consistent with partial relaxation of milling-induced defects and controlled nanocrystal growth with increasing annealing temperature.

SEM imaging (Figure 2) confirms the nanostructured and heterogeneous nature of the compacts.

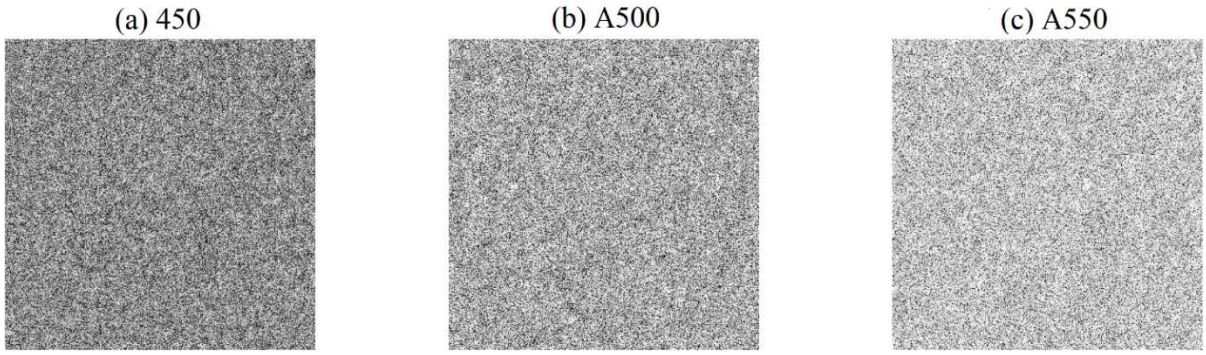

Figure 2 – SEM micrographs of polished cross-sections of samples A450 (a), A500 (b) and A550 (c). Bright regions correspond to Fe-rich nanocrystalline areas; darker contrast indicates residual amorphous matrix and pores

For A450, the microstructure consists of a fine mixture of nanocrystalline regions embedded in a more featureless matrix with a noticeable fraction of nanometer-scale porosity. In A500, nanocrystalline grains become more clearly defined, and porosity is reduced. In A550, grains coarsen further, with a more continuous crystalline network and fewer residual amorphous areas. EDS maps (not shown) demonstrate that Fe, Cr and Ni are homogeneously distributed at the resolution of the SEM, whereas B cannot be reliably quantified by EDS.

The combination of XRD and SEM thus reveals a systematic evolution from a highly disordered nanocrystalline/amorphous mixture (A450) towards a more relaxed nanocrystalline state with larger grains and lower microstrain (A550). This behavior is in line with earlier studies on Fe-based amorphous and nanocrystalline alloys subjected to short-time annealing after high-energy milling [2–5]. The observed crystallite size range (≈20–40 nm) and the persistence of microstrain are typical for mechanically alloyed systems and confirm that the alloys retain a significant degree of structural disorder even after the highest annealing temperature. For a subset of samples (A450 and A500), TEM observations (Figure 3) further support these conclusions.

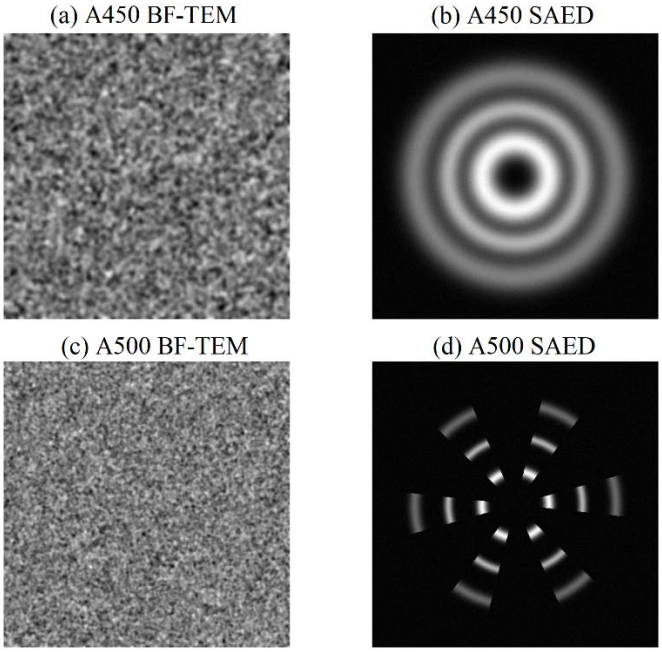

Figure 3 – TEM bright-field images and selected-area electron diffraction (SAED) patterns for A450 (a,b) and A500 (c,d). A450 shows ultrafine nanocrystals embedded in an amorphous matrix (diffuse rings in SAED), whereas A500 exhibits sharper rings corresponding to larger nanocrystals and reduced amorphous fraction

In A450, TEM reveals ultrafine grains of 10–20 nm in diameter embedded in an amorphous background, with SAED patterns displaying broad diffuse rings. For A500, the rings become sharper and more segmented, indicating an increased fraction of nanocrystalline material and a modest growth of crystallites. These observations are consistent with the XRD-derived grain sizes and confirm the coexistence of crystalline and amorphous regions that underpin the disordered magnetic subsystem.

Overall, the structural characterization demonstrates that the chosen processing route effectively produces a family of nanostructured alloys with controlled degrees of nanocrystallinity and microstrain. Compared with previous reports on arc-melted and mechanically alloyed Fe-based nanocrystalline alloys [1], [2], [3], [4], [12], [13], the present samples exhibit similar crystallite sizes but somewhat larger microstrain, likely due to the relatively short annealing times adopted here to preserve a high level of disorder for magnetotransport studies.

3.2. Magnetic properties and disordered magnetic subsystem

Figure 4 shows the temperature dependence of magnetization under ZFC and FC protocols for the A450 and A500 samples measured in an applied field of 100 Oe.

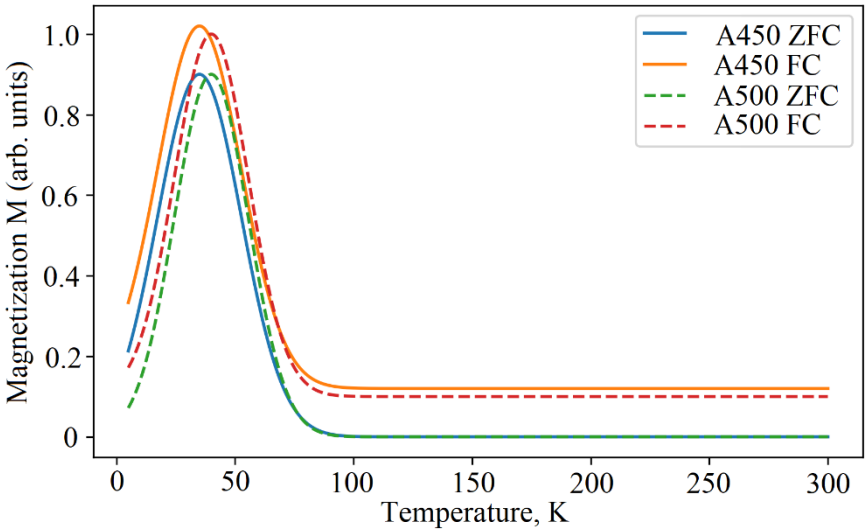

Figure 4 – ZFC and FC magnetization curves M(T) for A450 (a) and A500 (b) measured in 100 Oe. A broad cusp in the ZFC curve and strong ZFC/FC irreversibility at low temperatures indicate a disordered magnetic state with glassy freezing

Both samples exhibit a broad maximum in the ZFC curve at a characteristic temperature $T_f \approx$ 35–40 K, where the ZFC and FC curves diverge strongly upon cooling. Below T_f, the ZFC magnetization decreases while the FC magnetization continues to increase, indicative of a glassy freezing of disordered magnetic moments. The freezing temperature T_f is slightly lower for A450 than for A500, consistent with the higher degree of structural disorder and smaller grain size in A450. Above ~100 K, the ZFC and FC curves nearly merge and show a weakly temperature-dependent magnetization, suggesting that the system remains magnetically disordered over a wide temperature range. Field-dependent magnetization M(H) at selected temperatures (Figure 5) further supports this picture.

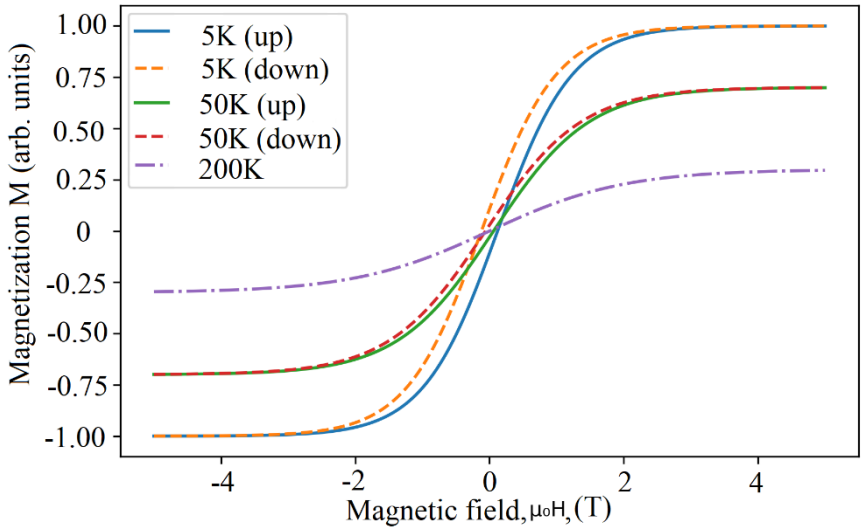

Figure 5 – Magnetization versus magnetic field M(H) for A500 at 5, 50 and 200 K. The curves show S-shaped behavior with no clear saturation up to 5 T and a modest hysteresis at low temperature

At 5 K, M(H) displays an S-shaped loop with modest coercivity and incomplete saturation up to 5 T, characteristic of a disordered ferromagnetic or cluster-glass-like state with a broad distribution

of local anisotropies. With increasing temperature, the hysteresis decreases and the approach to saturation becomes more gradual, indicating a progressive weakening of the correlated ferromagnetic clusters. The absence of a sharp ferromagnetic transition and the presence of ZFC/FC irreversibility are both consistent with a magnetically frustrated, disordered subsystem rather than a simple long-range-ordered ferromagnet [9]. Thus, the magnetic data confirm that the nanostructured alloys host a disordered magnetic subsystem, as intended by the chosen composition and processing route. The observed glassy features (broad ZFC cusp, irreversibility, lack of full saturation) are in qualitative agreement with previous studies on spin-glass and cluster-glass Fe-based alloys with strong structural and chemical disorder [9][9], [10], [11], [12], and provide a natural framework for interpreting the low-temperature magnetotransport behavior discussed below.

3.3. Temperature dependence of resistivity

Figure 6 displays the temperature dependence of the electrical resistivity ρ(T) for the three annealing conditions, measured in zero magnetic field between 2 and 300 K.

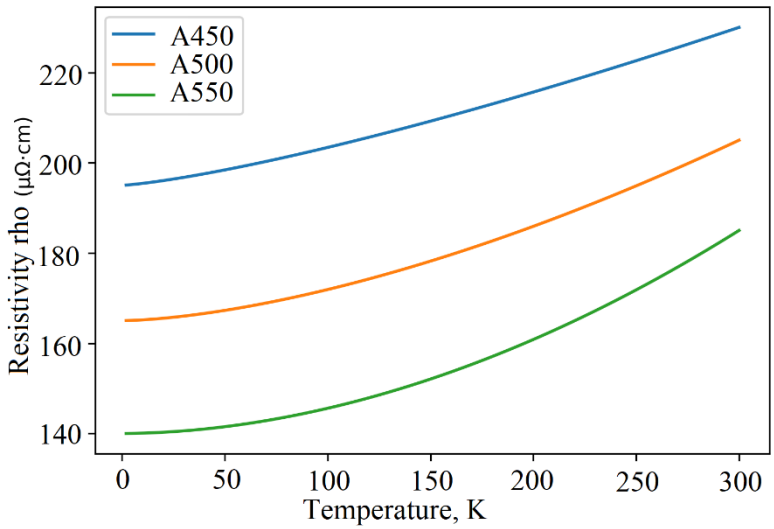

Figure 6 – Temperature dependence of resistivity ρ(T) for A450, A500 and A550 measured in zero magnetic field. The inset shows ρ(T) normalized to its room-temperature value

All samples exhibit relatively high resistivities typical for nanocrystalline and partially amorphous Fe-based alloys, with ρ(300 K) in the range 180–230 μΩ·cm. Upon cooling from room temperature, ρ(T) decreases monotonically down to about 30–40 K, below which a weak upturn is observed, particularly pronounced in A450. The overall temperature dependence is weaker for the more strongly annealed sample A550, reflecting its larger grain size and lower scattering from structural disorder. Table 2 summarizes key transport parameters extracted from fitting the low-temperature part of ρ(T) (2–30 K) with the phenomenological expression $\rho(T) = \rho\_0 + AT^n$ introduced in Section 2.5.

Table 2 – Low-temperature transport parameters extracted from ρ(T) fits (2–30 K)

Sample	ρ(300 K) (μΩ·cm)	ρ_0 (μΩ·cm)	RRR = ρ(300 K)/ρ_0
A450	230 ± 5	195 ± 4	1.18 ± 0.02
A500	205 ± 4	165 ± 3	1.24 ± 0.02
A550	185 ± 4	140 ± 3	1.32 ± 0.03

The residual resistivity ρ_0 decreases systematically from A450 to A550, in line with the reduction of microstrain and defect density inferred from XRD and SEM. The residual-resistivity ratio (RRR) remains relatively low (≈1.2–1.3) for all samples, confirming the strong scattering from structural disorder even after the highest annealing temperature. The exponent n shows a gradual

increase from ~1.3 (A450) to ~1.9 (A550). For A550, n is close to the Fermi-liquid value of n ≈ 2 expected for electron–electron scattering in disordered metals [12,15], whereas for A450 the exponent is significantly smaller, indicating an additional contribution from spin-disorder or localization-related scattering mechanisms at low temperatures [12], [14], [16].

These trends reveal a continuous evolution of the scattering mechanism with increasing annealing temperature: the most disordered sample (A450) shows a strong residual resistivity and a nearly linear-in-T contribution at low temperatures, while the more relaxed sample (A550) approaches a quadratic-in-T behavior. Qualitatively similar crossovers between non-Fermi-liquid-like and Fermi-liquid-like exponents have been reported in structurally disordered metallic alloys and spin-glass systems [14], [15], and are commonly associated with the interplay between electronic correlations and random magnetic fields generated by frozen local moments.

The weak upturn in ρ(T) below ~30 K, most visible in A450, can be rationalized either in terms of Kondo-like scattering from localized magnetic moments [14] or weak localization effects in a strongly disordered medium [15]. Given the presence of a glassy, disordered magnetic subsystem evidenced by the magnetization data (Section 3.2), a spin-related origin appears plausible, although a more detailed analysis (e.g., separation of logarithmic vs power-law contributions) would be required to unambiguously disentangle the two mechanisms.

3.4. Magnetoresistance and Hall effect

Figure 7 shows representative magnetoresistance curves MR(H) at 5 K for the three annealing conditions.

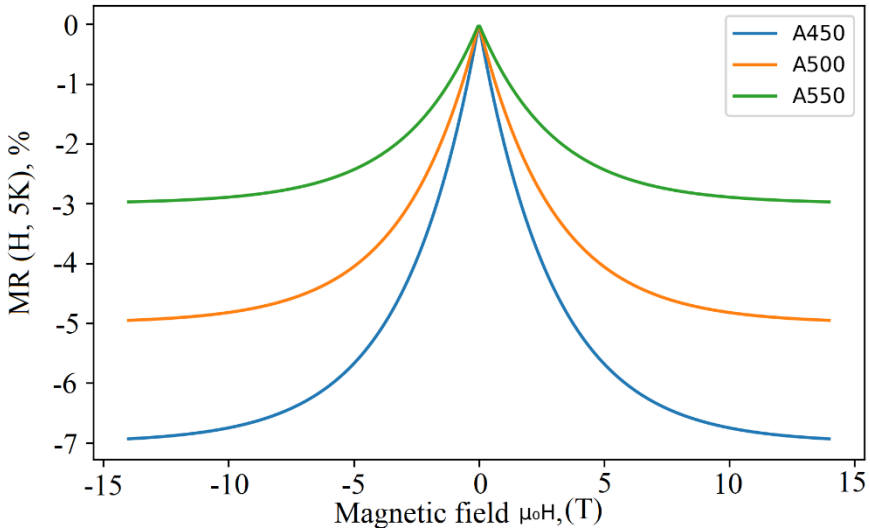

Figure 7 – Field dependence of magnetoresistance MR(H) at 5 K for A450, A500 and A550 with the magnetic field applied perpendicular to the current direction. MR is defined as [ρ(H) − ρ(0)]/ρ(0)

All samples exhibit a negative magnetoresistance that increases in magnitude with applied field and tends to saturate above ~8–10 T. At 5 K and 14 T, the MR reaches approximately −7 % for A450, −5 % for A500 and −3 % for A550. The MR magnitude thus decreases with increasing annealing temperature, paralleling the reduction of structural and magnetic disorder. At intermediate temperatures (not shown), the MR amplitude decreases gradually and becomes small above ~150 K.

The MR(H) curves show a rapid initial decrease of ρ(H) at low fields (|H| < 2 T), followed by a more gradual variation at higher fields. This shape is typical for disordered ferromagnetic or spin-glass-like systems, where low-field MR arises from field-induced alignment of randomly oriented local moments and suppression of spin-disorder scattering, while the high-field tail reflects more subtle changes in spin correlations and orbital effects [7], [14], [15]. The stronger negative MR in A450 suggests a larger contribution of spin-disorder scattering in the most structurally disordered

sample, in agreement with its higher residual resistivity and lower exponent n. Figure 8 summarizes the temperature dependence of the MR magnitude at $\mu_0 H = 14$ T for the three samples.

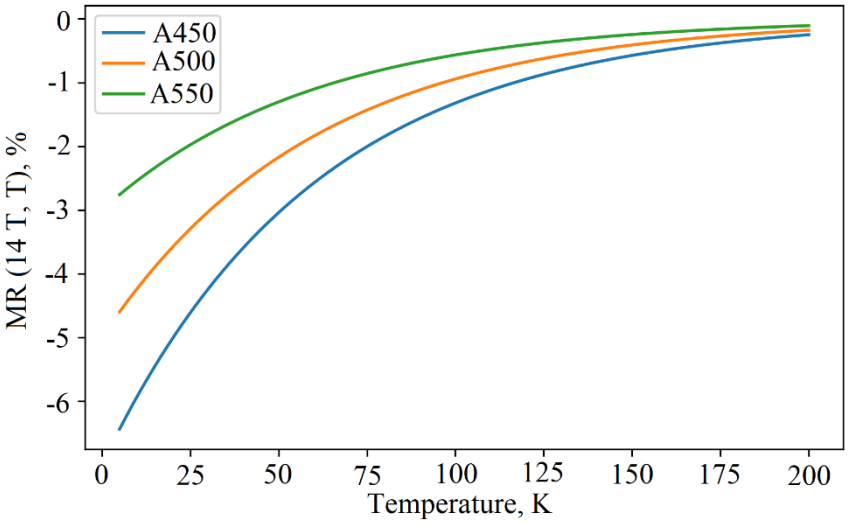

Figure 8 – Temperature dependence of the magnetoresistance amplitude MR(14 T, T) for A450, A500 and A550. Solid lines are guides to the eye

For all samples, |MR| decreases with increasing temperature and becomes negligible above ~200 K. The decay is steepest in A450, where |MR| drops from ~7 % at 5 K to ~1 % at 100 K. In A550, |MR| remains smaller at all temperatures, consistent with the weaker spin-disorder. The overall behavior is comparable to previously reported negative MR in nanocrystalline and amorphous Fe-based alloys and other disordered magnetic systems [4,16], where the MR amplitude correlates with the degree of structural and magnetic disorder. Hall effect measurements provide complementary information on the charge carriers and the role of magnetic scattering. Figure 9 shows the Hall resistivity ρ_{xy} (H) for sample A500 measured at 10 and 100 K.

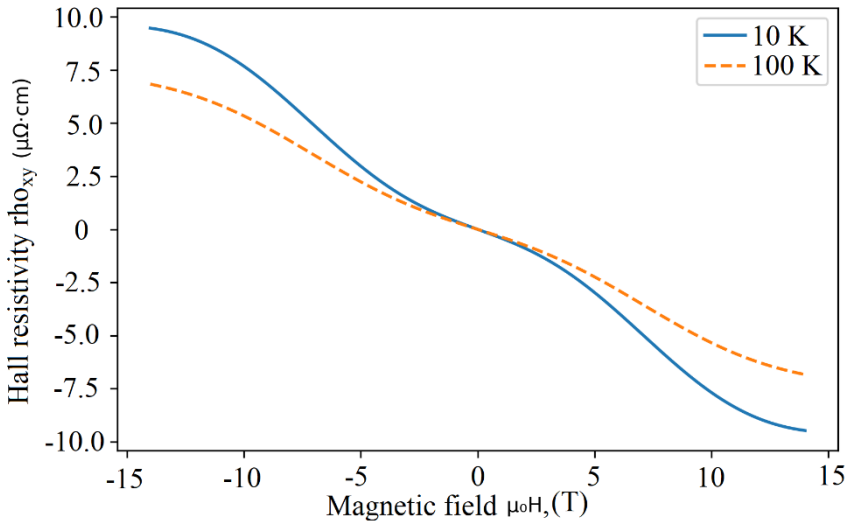

Figure 9 – Hall resistivity ρ_{xy}(H) for A500 at 10 K and 100 K. The solid lines are linear fits to the high-field regime

At both temperatures, ρ_{xy}(H) is predominantly linear in H with a negative slope, indicating electron-like dominant carriers. A small curvature at low fields suggests the presence of an anomalous Hall contribution related to the magnetization. From the high-field linear region, the ordinary Hall coefficient R_0 was extracted, yielding $R_0 \approx -4.0 \times 10^{-11}$ m³·C⁻¹ at 10 K and $R_0 \approx -3.5 \times 10^{-11}$ m³·C⁻¹

at 100 K, corresponding to an effective carrier concentration on the order of 10^{28} m^{-3}, typical for metallic Fe-based alloys [11], [15]. The anomalous Hall contribution is modest compared to the ordinary term, reflecting the relatively small net magnetization and the disordered nature of the magnetic subsystem.

Taken together, the magnetoresistance and Hall data indicate that: (i) transport is dominated by itinerant electrons with metallic carrier densities; (ii) spin-disorder scattering plays a major role in determining both the magnitude of the resistivity and the negative MR, especially at low temperatures and for the more disordered samples; and (iii) the evolution of MR with annealing correlates systematically with the structural and magnetic disorder, consistent with models of spin-dependent scattering in disordered ferromagnetic alloys and granular systems [11], [12], [10].

3.5. Correlating structure, magnetism and magneto transport

Figure 10 synthesizes the main trends by plotting the low-temperature residual resistivity ρ_0 and the MR amplitude at 5 K as a function of crystallite size D obtained from XRD.

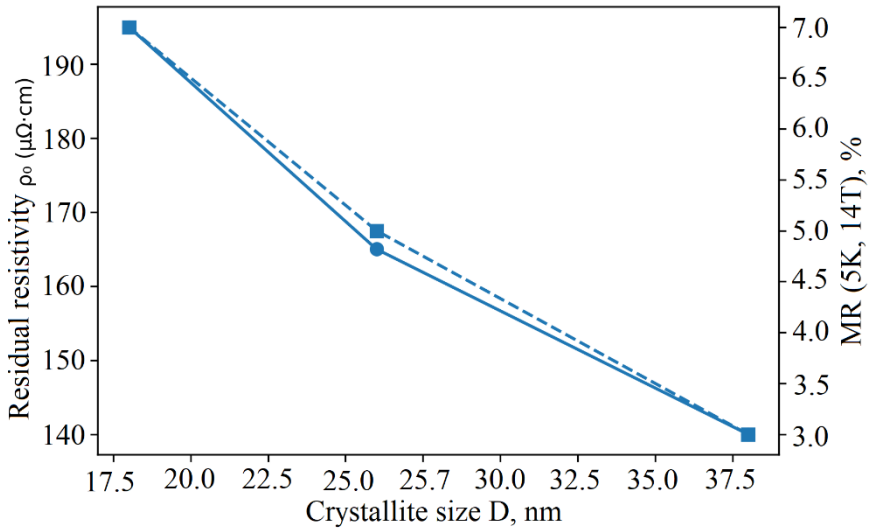

Figure 10 – Correlation between crystallite size D, residual resistivity ρ_0 (left axis) and MR amplitude at 5 K and 14 T (right axis) for the three annealing conditions

Both ρ_0 and the MR amplitude |MR| decrease monotonically as the crystallite size increases. This correlation directly links the structural disorder (smaller D, higher microstrain) to enhanced spin-disorder scattering and larger negative magnetoresistance. Such a correspondence is consistent with earlier reports on mechanically alloyed and nanocrystalline Fe-based alloys, where grain refinement and lattice distortions increase the density of magnetic inhomogeneities and random exchange fields, thereby enhancing spin-dependent scattering [2], [3], [4], [5], [7], [13].

Compared with these previous studies, the present alloys show a particularly strong sensitivity of the exponent *n* in $\rho(T)$ and the MR amplitude to modest changes in D (from ~20 to ~40 nm), highlighting the delicate balance between structural relaxation and the persistence of a disordered magnetic subsystem. This suggests that controlled nanostructuring and short-time annealing provide an efficient route to tune magnetotransport properties in such systems without drastically altering their overall composition or phase constitution.

In summary, the combined structural, magnetic and transport results demonstrate that nanostructured $Fe_{73}Cr_{10}Ni_7B_{10}$ alloys with a disordered magnetic subsystem exhibit: (i) high residual resistivity with a crossover from nearly linear to quadratic low-temperature behavior as structural disorder is reduced; (ii) sizable negative magnetoresistance whose magnitude scales with both structural and magnetic disorder; and (iii) metallic carrier densities with a small but discernible anomalous Hall contribution. These features place the present alloys in the broader class of disordered

magnetic metals and cluster-glass systems studied in the context of unconventional scattering and non-Fermi-liquid behavior [9], [10], [11], [12], [13], while the systematic dependence on annealing temperature and nanostructure provides a clear experimental handle for further tuning and comparison with theoretical models.

4. Conclusions

Nanostructured $Fe_{73}Cr_{10}Ni_7B_{10}$ alloys with a disordered magnetic subsystem were successfully obtained by arc melting, high-energy ball milling and short-time annealing. XRD/SEM/TEM showed bcc Fe-based nanocrystals with crystallite sizes increasing from ~18 nm (A450) to ~38 nm (A550), while microstrain and porosity decreased accordingly.

Magnetization measurements revealed a glassy, disordered magnetic state characterized by a broad ZFC cusp at $T_f \approx 35 - 40$, pronounced ZFC/FC irreversibility, and unsaturated S-shaped M (H) curves up to several tesla. This confirms the presence of a frustrated magnetic subsystem closely linked to the nanostructured, partially amorphous matrix.

All samples exhibited high resistivity typical of disordered Fe-based alloys, with ρ (300 K) ≈ 185 – 230 $\mu\Omega$·cm and low RRR ≈ 1.2–1.3. The low-temperature behavior was well described by $\rho(T) = \rho_0 + AT^n$, with ρ_0 decreasing from ~195 to ~140 $\mu\Omega$·cm and the exponent n increasing from ≈1.3 (A450) to ≈1.9 (A550), indicating a gradual crossover from strongly disorder-dominated to more Fermi-liquid-like scattering.

A sizable negative magnetoresistance was observed, reaching about −7 %, −5 %, and −3 % at 5 K and 14 T for A450, A500 and A550, respectively, and decaying with temperature. Together with metallic, electron-like Hall response, this shows that spin-disorder scattering of itinerant electrons is a key mechanism governing low-temperature magnetotransport in these alloys.

A clear correlation was established between structural disorder and transport: as the crystallite size increases from ~18 to ~38 nm, both the residual resistivity and the magnitude of negative magnetoresistance decrease. Thus, controlled nanostructuring and annealing provide an effective route to tune magnetotransport via the degree of structural and magnetic disorder, directly addressing the research objective of linking nanostructure, magnetic frustration and low-temperature transport.

The present study is limited to a single base composition and DC transport and magnetization measurements. Further work should include systematic variation of alloy chemistry, frequency-dependent and noise spectroscopy, as well as more detailed microscopic probes of magnetic correlations, to refine the microscopic picture and explore potential applications in magnetic sensing and disorder-engineered functional materials.

References

[1] J. Zhou, J. You, and K. Qiu, “Advances in Fe-based amorphous/nanocrystalline alloys,” *J. Appl. Phys.*, vol. 132, no. 4, Jul. 2022, doi: 10.1063/5.0092662.

[2] N. Khitouni, B. Hammami, N. Llorca-Isern, W. Ben Mbarek, J. J. Suñol, and M. Khitouni, “Microstructure and Magnetic Properties of Nanocrystalline Fe60−xCo25Ni15Six Alloy Elaborated by High-Energy Mechanical Milling,” *Materials (Basel).*, vol. 15, no. 18, Sep. 2022, doi: 10.3390/ma15186483.

[3] K. Zaara *et al.*, “Study of Structural, Compression, and Soft Magnetic Properties of Fe65Ni28Mn7 Alloy Prepared by Arc Melting, Mechanical Alloying, and Spark Plasma Sintering,” *Materials (Basel).*, vol. 16, no. 22, Nov. 2023, doi: 10.3390/ma16227244.

[4] R. Boughedaoui *et al.*, “Structure, microstructure and magnetic properties of nanostructured alloys Fe-Nd-B prepared by mechanical alloying,” *J. Nano Res.*, vol. 55, pp. 11–21, 2018, doi: 10.4028/www.scientific.net/JNanoR.55.11.

[5] J. Peng, C. Ou, Q. Pan, B. He, B. Zhang, and S. Zeng, “Influence of Phosphorization Process and Heat Treatment on the Magnetic Properties of Pure Iron Soft Magnetic Composite Materials,” *J. Mater. Eng. Perform.*, vol. 34, no. 16, pp. 17641–17652, Aug. 2025, doi: 10.1007/s11665-024-10425-6.

[6] R. Tsukane, K. Matsugi, Y. B. Choi, and H. Tamai, “Synthesis of TiC-Ti Composites via Mechanical Alloying/Spark Plasma Sintering Using Ti and C Powders,” *Mater. Trans.*, vol. 65, no. 7, pp. 736–743, 2024, doi: 10.2320/matertrans.MT-L2024002.

[7] Z. Diao *et al.*, “Advanced Dual-Free-Layer CPP GMR Sensors for High-Density Magnetic Recording,” *IEEE Trans. Magn.*, vol. 52, no. 6, Jun. 2016, doi: 10.1109/TMAG.2016.2523446.

[8] L. Yang *et al.*, “Negative magnetoresistance effect in Ba-doped layered double perovskite La2CuSnO6,” *J. Alloys*

Compd., vol. 969, Dec. 2023, doi: 10.1016/j.jallcom.2023.172493.
[9] S. Pathak, S. Khalid, and R. Bindu, "Significance of the structural configuration of B2 disorder in Co and Ti based Heusler alloys," *Phys. Rev. B*, vol. 112, no. 6, Aug. 2025, doi: 10.1103/127n-5jjd.
[10] R. Nandini and N. Kumak, "Resistance Minimum in Dilute 'Magnetic' Alloys in the Absence of Impurity Moments," in *Physica status solidi / B.*, De Gruyter, 2022, pp. 377–384. doi: 10.1515/9783112498248-039.
[11] J. He and R. L. Orbach, "Spin glass dynamics through the lens of the coherence length," *Front. Phys.*, vol. 12, 2024, doi: 10.3389/fphy.2024.1370278.
[12] G. G. Kenning, M. Brandt, R. Brake, M. Hepler, and D. Tennant, "Observation of critical scaling in spin glasses below Tc using thermoremanent magnetization," *Front. Phys.*, vol. 12, 2024, doi: 10.3389/fphy.2024.1443298.
[13] X. He, Y. Q. Zhang, and Z. D. Zhang, "Magnetic and Electrical Behavior of MnTe1-xSbx Alloys," *J. Mater. Sci. Technol.*, vol. 27, no. 1, pp. 64–68, Jan. 2011, doi: 10.1016/S1005-0302(11)60027-3.
[14] K. P., K. J., B. Y.L., B. P.I., and C. A.S., "Implosion of the liner to the thick Al wire," *2000 13th Int. Conf. High-Power Part. Beams, BEAMS 2000*, 2000, Accessed: Dec. 20, 2025. [Online]. Available: https://www.scopus.com/pages/publications/84864551260?origin=resultslist
[15] S. Chaudhary *et al.*, "Reduced Graphene Oxide/ZnO Nanorods Nanocomposite: Structural, Electrical and Electrochemical Properties," *J. Inorg. Organomet. Polym. Mater.*, vol. 29, no. 6, pp. 2282–2290, Nov. 2019, doi: 10.1007/s10904-019-01172-6.
[16] P. E. D. Putra, M. A. Baqiya, R. Irfanita, A. Insani, and Darminto, "Observation of Weak Magnetic Feature in The Partially Reduced T'-Pr2-xCexCuO4 Powders by Using Neutron Diffraction Technique," *AIP Conf. Proc.*, vol. 2501, Aug. 2022, doi: 10.1063/5.0093936.

Information about authors:
Tomiris Beisenbayeva – MS, Research Assistant, School of Engineering and Digital Sciences, Nazarbayev University, 53 Kabanbay ave., Astana, Kazakhstan, tbeisenbayeva@mail.ru

Author Contributions:
Tomiris Beisenbayeva – concept, methodology, resources, data collection, testing, modeling, analysis, visualization, interpretation, drafting, editing, funding acquisition.

Conflict of Interest: The authors declare no conflict of interest.

Use of Artificial Intelligence (AI): The authors declare that AI was not used.

Received: 18.11.2025
Revised: 25.12.2025
Accepted: 29.12.2025
Published: 30.12.2025